Stanford Exploration Project, Report 105, September 5, 2000, pages 123–??

Daylight imaging in $V(x, y, z)$ media

Gerard T. Schuster and James Rickett[1]

ABSTRACT

Previous authors have tried to image seismic reflectivity by crosscorrelating passive seismic data, and treating the resultant correlograms as active source seismograms. We provide a mathematical framework for working with passive seismic correlograms that is both appropriate for $V(x, y, z)$ media, and arbitrary source location. Under this framework, correlograms can be migrated with an imaging condition that is tuned to image particular events. For example, tuning the imaging condition to the kinematics of the *Direct-Direct* correlation event allows direct imaging of the seismic sources. Similarly, tuning to the *Direct-Ghost* correlation event allows imaging of subsurface reflectivity. Numerical results with synthetic data partly verify the effectiveness of crosscorrelation migration, but also suggest worse resolution of the image compared to standard Kirchhoff migration.

INTRODUCTION

Passive seismic imaging can be split into two categories: firstly, attempts to image the spatial locations of passive seismic sources themselves, and secondly, attempts to image the subsurface reflectivity that is illuminated by passive seismic energy.

Passive seismic source imaging

Passive seismic source imaging has the unique potential to provide direct measurements of subsurface permeability [e.g. Shapiro et al. (1999)]. Fluid flow causes fracturing; you image the fracturing; therefore, you are imaging the fluid flow. This, along with the growth of (both surface and borehole) time-lapse seismic, has led to the drive towards the "electric oilfield" permanently instrumented and continually monitoring itself (Jack and Thomsen, 1999).

To date, however, most of the published case studies of microseismic fracture imaging rely on earthquake-style hypocentral event triangulation. For example, Maxwell et al. (1998) describe the successful application of such technology to the Ekofisk field in the North Sea. These approaches require automated event picking algorithms, and may run into problems if microseismic events are not localized in time.

[1] **email:** schuster@mines.utah.edu, james@sep.stanford.edu

Reflectivity imaging with passive seismic energy

Baskir and Weller (1975) describe possibly the first published attempt to use passive seismic energy to image subsurface reflectivity. They briefly describe crosscorrelating long seismic records to produce correlograms that could be processed, stacked and displayed as conventional seismic data. Unfortunately their field tests seem to have been inconclusive.

Dating from about the same time, an exercise in Claerbout's first book (1976) asks the reader to prove that the temporal autocorrelation of a transmission seismogram with a source deep underground is equivalent to a reflection seismogram. This may have inspired his conjecture that by crosscorrelating two passive traces, we can create the seismogram that would be computed at one of the locations if there was a source at the other. Cole (1995) attempted to verify this conjecture with data collected using a 4000 channel 2-D field array on Stanford campus. Unfortunately, again, possibly due to the short (20 minute) records or bad coupling between the geophones and the dry California soil, his results were inconclusive.

Following Cole's work, Rickett and Claerbout (1996) generated synthetic data with a phase-shift method. Their earth reflectivity models consisted of (both flat and dipping) planar layers and point diffractors embedded in a $v(z)$ velocity function, and illuminated by random plane waves from below. They generated both *pseudo shot gathers* (by crosscorrelating one passive trace with many others nearby), and *pseudo zero-offset sections* (by autocorrelating many traces). In these crosscorrelated domains, the kinematics for both point diffractors and planar reflectors, were identical to those predicted for real shot gathers and zero-offset sections. Rickett (1996) then experimented with moving the passive source location close to the receivers and reflectors, and included modeling with a $v(x,z)$ velocity model. He observed that these changes did indeed affect the kinematics of the correlograms; however, changes were small, and would probably not cause the method to fail in most situations.

The idea that a pseudo-reflection seismogram could be created by crosscorrelating two passive seismic records was rediscovered independently by the helioseismologists Duvall et al. (1993), who created *time-distance* curves by cross-correlating passive solar dopplergrams recorded by the Michelson Doppler Imager (Scherrer et al., 1995). Point-to-point traveltimes derived from these time-distance curves could then be used in a range of helioseismic applications [e.g. Giles et al. (1997) and Kosovichev (1999)]. If helioseismic time-distance curves are averaged spatially, the result is equivalent to a multi-dimensional autocorrelation. Rickett and Claerbout (1999; 2000) demonstrated that multi-dimensional spectral factorization provides spatially averaged time-distance curves with more resolution than those calculated by autocorrelation.

Extending daylight imaging

In this paper, the daylight imaging method is represented mathematically and extended to image arbitrary reflectivity and source distributions in $v(x,y,z)$ media. We temporally crosscorrelate the traces to form *pseudo-shot* gathers. These gathers are then migrated according to a crosscorrelogram migration operator (Schuster, 1999). The migration operator can be tuned to image either the source locations, or the subsurface reflectivity distribution. Simple synthetic examples are given to clarify the benefits and limitations of this daylight imaging procedure. A special case of crosscorrelation migration is that of autocorrelation migration (Schuster et al., 2000; Yu et al., 2000), except that now the source location does not need to be known.

THEORY OF DAYLIGHT IMAGING

We will now describe how to image either the source distribution or the reflectivity distribution from passive seismic data in a $v(x,y,z)$ medium. The sources are assumed to be distributed anywhere in space, and the time histories of each source are assumed to be uncorrelated. Neither the source location or time history are known. Without loss of generality we conveniently assume one source and one scatterer, but the resulting migration formula are also applicable to multiple sources and scatterers.

For an earth model with a free-surface, a smoothly varying velocity distribution and a single point scatterer at x_o, the wavefield, $W(\vec{r}_{g'}|\vec{r}_s,\omega)$, recorded at $\vec{r}_{g'}$ due a source at $\vec{r}_s$ is given by

$$\begin{aligned} W(\vec{r}_{g'}|\vec{r}_s,\omega) &\approx G(\vec{r}_{g'}|\vec{r}_s,\omega)\; F(\omega), \\ &= \mathrm{H}ello[Direct_{g'} \;+\; Primary_{g'} \;+\; Ghost_{g'}]\; F(\omega), \\ &= [e^{i\omega\tau_{sg'}} + Re^{i\omega(\tau_{sx_o}+\tau_{x_o g'})} - Re^{i\omega(\tau_{sg''}+\tau_{g''x_o}+\tau_{x_o g'})}]\; F(\omega), \end{aligned} \tag{1}$$

where $G(\vec{r}_g|\vec{r}_s,\omega)$ is the WKBJ Green's function for an impulsive source at $\vec{r}_s$ and a geophone at $\vec{r}_g$, and $F(\omega)$ is the complex source spectrum.

The first term on the RHS represents the direct arrival (see top figure in Figure 1), the second term represents the scattered field excited by the direct arrival, and the third term represents the scattered arrival that is generated by a specular free-surface reflection (see middle figure in Figure 1). Here, R is the scattering coefficient, $\tau_{gg'}$ is a solution to the eikonal equation for a source at g and a receiver at g', and the geometrical-spreading factors have been harmlessly dropped. The specular-reflection point on the free surface is denoted by g'' and the location of the recording geophone is denoted by g'.

To eliminate the unknown phase of the source, we crosscorrelate the wavefield, $W(\vec{r}_{g'}|\vec{r}_s,\omega)$ recorded at $\vec{r}_{g'}$ with $W(\vec{r}_{g_o}|\vec{r}_s,\omega)$ recorded at $\vec{r}_{g_o}$ to get

$$W(\vec{r}_{g'}|\vec{r}_s,\omega)W(\vec{r}_{g_o}|\vec{r}_s,\omega)^* \;=\; G(\vec{r}_{g'}|\vec{r}_s,\omega)G(\vec{r}_{g_o}|\vec{r}_s,\omega)^*\;|F(\omega)|^2 \tag{2}$$

If we then assume source is a white source spectrum such that $|F(\omega)|^2 \approx 1$, the source term can be dropped entirely, leaving

$$\begin{aligned} W(\vec{r}_{g'}|\vec{r}_s,\omega)W(\vec{r}_{g_o}|\vec{r}_s,\omega)^* &= G(\vec{r}_{g'}|\vec{r}_s,\omega)G(\vec{r}_{g_o}|\vec{r}_s,\omega)^* \\ &= Direct_{g'}\; Direct_{g_o}{}^* \;+\; Ghost_{g'}\; Direct_{g_o}{}^* + other\ terms \\ &= e^{i(\omega\tau_{sg'}-\omega\tau_{sg_o})} - Re^{i\omega(\tau_{sg''}+\tau_{g''x_o}+\tau_{x_o g'}-\tau_{sg_o})} + other\ terms, \end{aligned} \tag{3}$$

where the first expression on the RHS corresponds to the correlation of the conjugate direct wave recorded at geophone g_o with the direct wave at g'; and the second term corresponds to the correlation of the conjugate direct wave at g_o with the ghost reflection recorded at g'. The *other terms* correspond to the other correlations which will not be needed for imaging, and are presumed to cancel upon migration. This last assumption about cancellation is similar to the standard assumption in migration, i.e., all migrated arrivals incoherently superimpose except those that are tuned to the specified imaging condition. For the above equation, we will tune the imaging conditions so that either the $Direct^*_{g_o}\ Direct_{g'}$ terms are migrated to image the source distribution, or the $Direct^*_{g_o}\ Ghost_{g'}$ terms are migrated to image the reflectivity distribution.

Source location imaging

To image the unknown source location at $\vec{r}_s$ from the data given in equation (3), we simply identify the migration operator which when applied to the above equation cancels the phase of the $Direct^*_{g_o}\ Direct_{g'}$ term. Such a migration operator is given by

$$e^{-i\omega(\tau_{s'g'}-\tau_{s'g_o})}, \tag{4}$$

where s' denotes the trial source-point location. Application of this migration operator to the crosscorrelated data in equation (3) will annihilate the phase of the $Direct^*_{g_o}\ Direct_{g'}$ term when the trial image point $\vec{r}_{s'}$ coincides with the actual source location denoted by $\vec{r}_s$. The migration section is then given by summation over all geophone pairs

$$\begin{aligned} m_{\text{source}}(\vec{r}_{s'},\omega) &= \sum_{g_o}\sum_{g'} W(\vec{r}_{g'}|\vec{r}_s,\omega)\, W(\vec{r}_{g_o}|\vec{r}_s,\omega)^*\, e^{-i\omega(\tau_{s'g'}-\tau_{s'g_o})}, \\ &= \sum_{g_o}\sum_{g'} \left[e^{i\omega(\tau_{sg'}-\tau_{sg_o}-\tau_{s'g'}+\tau_{s'g_o})} + \textit{all other terms} \right]. \end{aligned} \tag{5}$$

The migration operator in equation (5) is "tuned" to image the source location so that as $\vec{r}_{s'} \to \vec{r}_s$, the $Direct^*_o\ Direct_{g'}$ term will constructively interfere while the *all other terms* tend to cancel.

Reflectivity distribution imaging

To image the unknown scatterer location and strength at $\vec{x}_o$, we simply identify the migration operator which, when applied to the crosscorrelated data in equation (4), cancels the phase of the $Direct^*_{g_o}\ Ghost_{g'}$ term. Such a migration operator is given by

$$e^{-i\omega(\tau_{g_o x}+\tau_{xg'})}, \tag{6}$$

where x and g_o denote, respectively, the *trial* scatterer and specular-reflector point locations respectively. Application of this migration operator to equation (3) will annihilate the phase

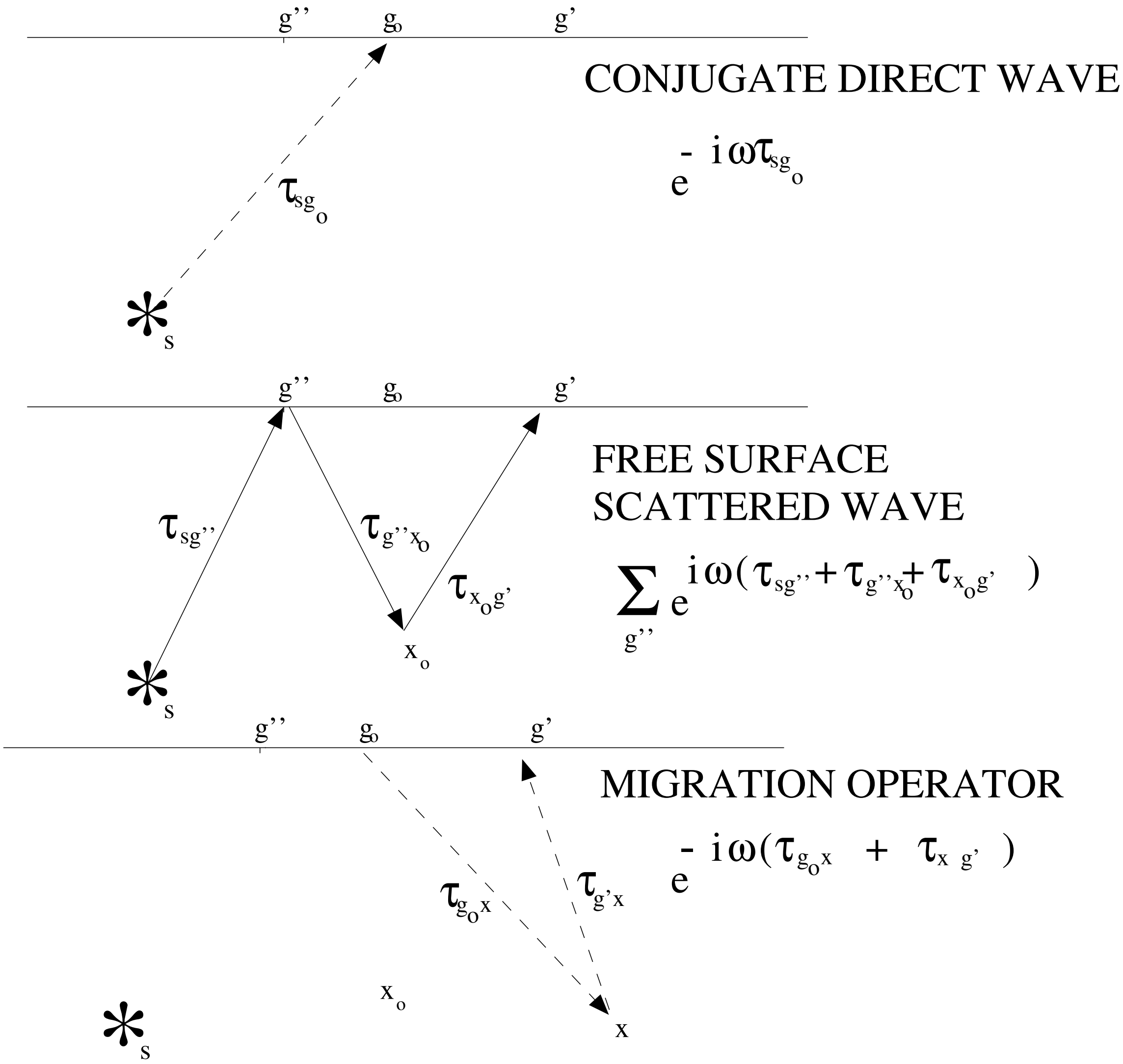

Figure 1: (Top) Direct ray and a (middle) scattered ray excited by a specular free-surface reflection associated with a source at s and a scatterer at x_o. Bottom figure denotes the rays associated with the migration operator for free-surface reflections. $\boxed{\text{schuster-fig1}}$ [NR]

term of the $Direct^*_{g_o}\ Ghost_{g''}$ term in equation (3) when both the trial image point, $\vec{x}$, coincides with the actual source location denoted by $\vec{x}_o$, *and* the trial specular-reflection point, $\vec{r}_{g_o}$, coincides with the actual specular-reflection point, $\vec{r}_{g''}$. In other words, we require both

$$\begin{aligned} \vec{x} &\rightarrow x_o, \text{ and} && (7)\\ \vec{r}_{g_o} &\rightarrow \vec{r}_{g''}. && (8) \end{aligned}$$

This can be understood more clearly by noting that the migrated reflectivity section is given by summation of the migrated crosscorrelation data over all geophone pairs

$$\begin{aligned} m_{\text{refl}}(\vec{x},\omega) &= \sum_{g_o}\sum_{g'} W(\vec{r}_{g'}|\vec{r}_s,\omega)\, W(\vec{r}_{g_o}|\vec{r}_s,\omega)^*\, e^{-i\omega(\tau_{g_o x}+\tau_{xg'})},\\ &= -R\sum_{g_o}\sum_{g'}\left[e^{i\omega(\tau_{sg''}+\tau_{g''x_o}+\tau_{x_o g'}-\tau_{sg_o}-\tau_{g_o x}-\tau_{xg'})} + \textit{all other terms}\right]. \end{aligned} \tag{9}$$

As $\vec{x} \rightarrow x_o$ and as $\vec{r}_{g_o} \rightarrow \vec{r}_{g''}$, then it is clear that the above phase goes to zero, leading to constructive interference at the scatterer's location. In practice, these two conditions will be fulfilled if the specular-reflection point is within the aperture of the recording array and the geophone array is sufficiently dense.

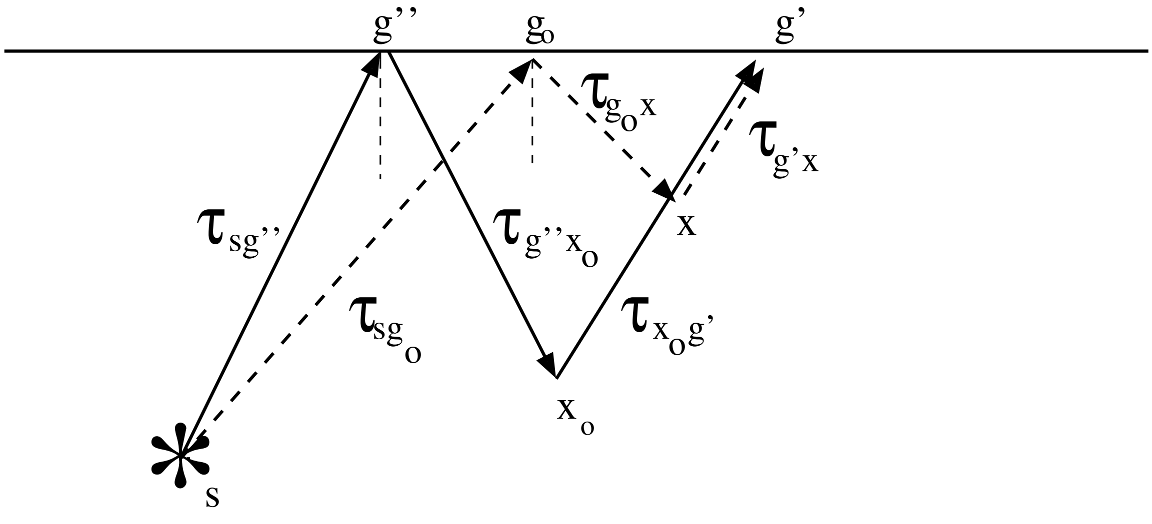

Figure 2: Ghost reflection rays associated with a source at s, a trial image point at x, and a scatterer at x_o. $\boxed{\text{schuster-fig2}}$ [NR]

NUMERICAL RESULTS

We generated synthetic data to test the feasibility of imaging the location of unknown sources and of imaging the reflectivity distribution from free-surface multiples. The first example imitates the scenario where a fluid is injected into a medium to open cracks, and the goal is to use

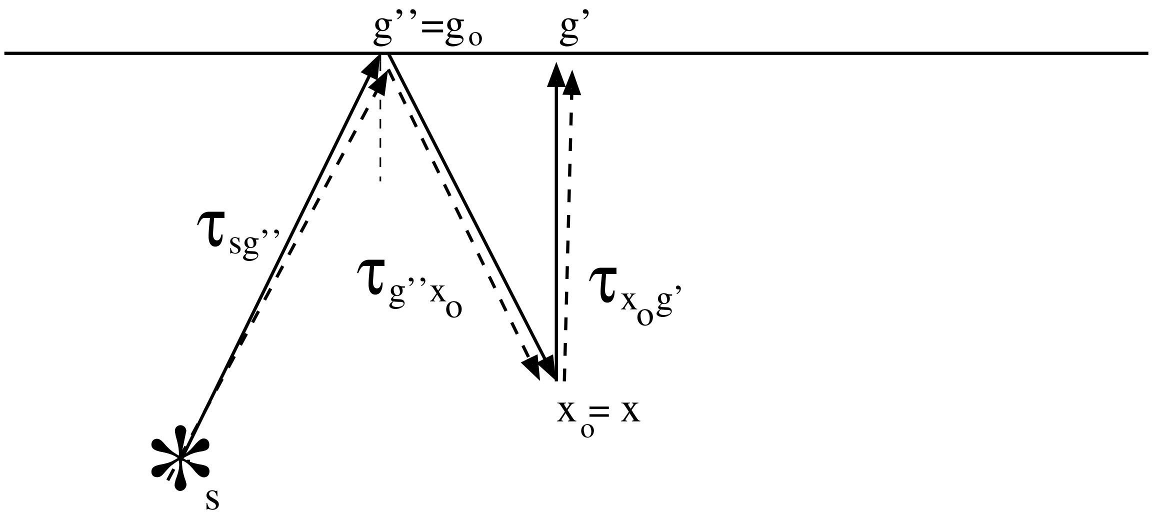

Figure 3: As x approaches x_0 and g_o approaches g'' in Figure 2, the dashed rays coincide with the solid rays. Thus the *Direct Ghost* correlation term will have zero phase, leading to maximal constructive interference of the migration section at the actual scatterer point. schuster-fig3 [NR]

passive seismic data to image the location of the opened cracks. The second example approximates the situation where the reflectivity distribution is imaged from seismic data generated by a drill bit with unknown location.

Imaging the location of seismic sources

The top panel of Figure 4 shows synthetic data generated for a point exploder embedded in a constant velocity medium centered 1050 m below a 2100 m wide array. There are 70 geophones in the array with a geophone spacing of 30 m. The traces are computed for 1 second of duration with a 30 Hz Ricker wavelet source. The point scatterer response of the Kirchhoff operator and the crosscorrelation migration operator in equation (4) are shown in the middle and lower panels of Figure 4, respectively.

Note, the crosscorrelation image of the point scatterer is smeared over a larger depth range than that of the Kirchhoff image. This is because the crosscorrelation of one trace with another smears the source wavelet into a longer wavelet, and also because the crosscorrelation operator has poor resolution in the depth direction (see Figure 5). Nevertheless, the crosscorrelation point-scatterer image is acceptable.

In practice, the master trace and its two nearest neighbors were muted because the direct wave migration operator in equation (4) has zero or nearly zero phase when $g \approx g'$. This is undesirable because any energy from these traces will be smeared uniformly throughout the model, not just at the exploder points. Also, a second derivative in time was applied to the crosscorrelogram traces to partly compensate for the smoothing effects of crosscorrelation and migration.

Figure 5 is the same as Figure 4 except the source wavelet is a long random time series. The crosscorrelation of traces collapses the ringy time series to an impulse-like wavelet so that the associated migration image in the lower panel of Figure 5 has good spatial resolution compared to the Kirchhoff image in the middle panel.

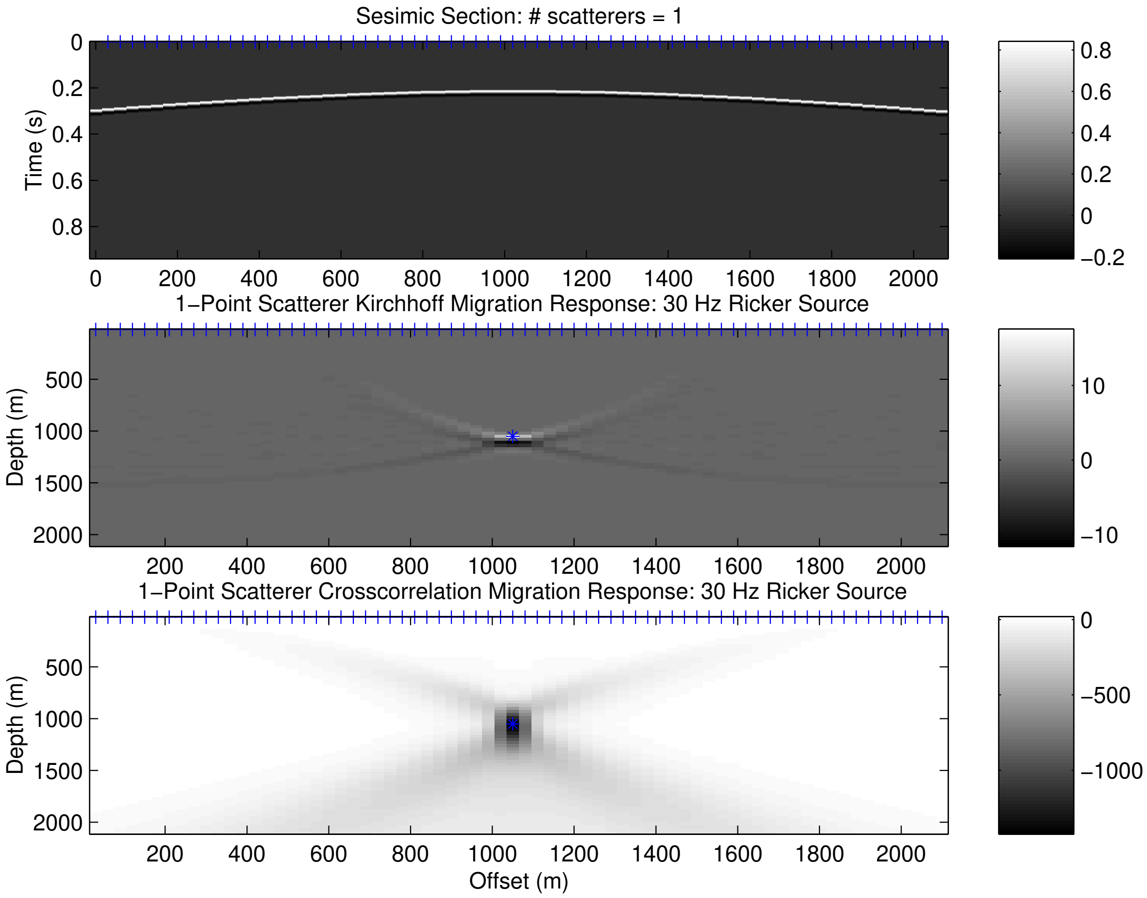

Figure 4: Source imaging test with 30 Hz impulsive source at a depth of 1050 m and $t = 0$: The top panel shows the synthetic data. The middle panel shows the Kirchhoff migration image, and lower panel shows crosscorrelation migration image. The true image location is marked by an asterisk (*). The Kirchhoff image is better resolved than the crosscorrelation image partly because the temporal crosscorrelation broadens the seismic wavelet. schuster-fig4 [NR]

In the previous examples, the scatterer exploded at time zero. Figure 6 shows a similar synthetic experiment with ten scatterers, all exploding at random times with a random time series as a source wavelet. The resulting data for 1 second is shown in the top panel of Figure 6. The middle panel shows these data after crosscorrelation migration of 1 second of data, and roughly locates the location of the 10 point sources. Repeating this crosscorelation migration for fifteen data sets, each with 1 second of data generated from ten point scatterers with distinct random time histories, yields the stacked images shown in the lower panel of Figure 6. As expected, averaging the migration images tends to cancel migration noise and reinforce the energy at the location of the point exploders.

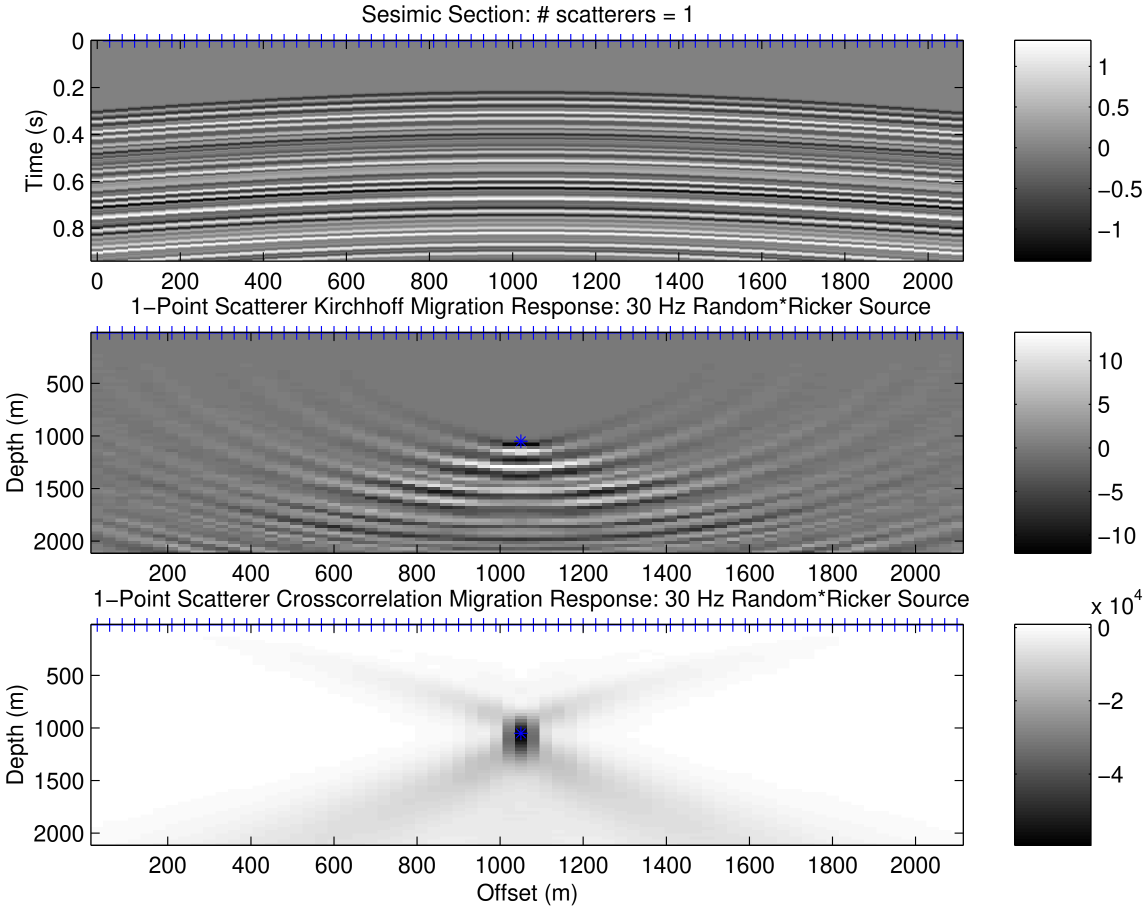

Figure 5: Same as Figure 4, except the source wavelet is a long random time series beginning at $t = 0$. The top panel shows the synthetic data. The middle panel shows the Kirchhoff migration image, and lower panel shows crosscorrelation migration image. The true image location is marked by an asterisk (*). Note that the crosscorrelation of traces collapses the ringy source wavelet into an impulsive-like wavelet, leading to a better resolved migration image in the crosscorrelogram image. schuster-fig5 [NR]

Finally, the fault-like structure denoted by stars in Figure 7 is assumed to emanate seismic energy randomly in time with random strength. This might approximate the situation where fluid is injected along a reservoir bed and seismic instruments are passively monitoring the injection front. Figure 7 shows the results after crosscorrelation migration of 1 second of data (middle panel), and 40 stacks of 1 second records (lower panel). The fault boundaries are much better delineated in the 40-stack migration image, although the resolution is much worse than that of an ordinary seismic survey.

Poor resolution of the crosscorrelation images is consistent with theoretical predictions of resolution for crosscorrelation migration operators. A possibility for improving resolution is to measure the incidence angle of energy in the correlograms and use this angle as a constraint in smearing data into the model. This strategy is similar to that of ray-map migration, but it remains to be seen if this is a practical strategy with correlograms.

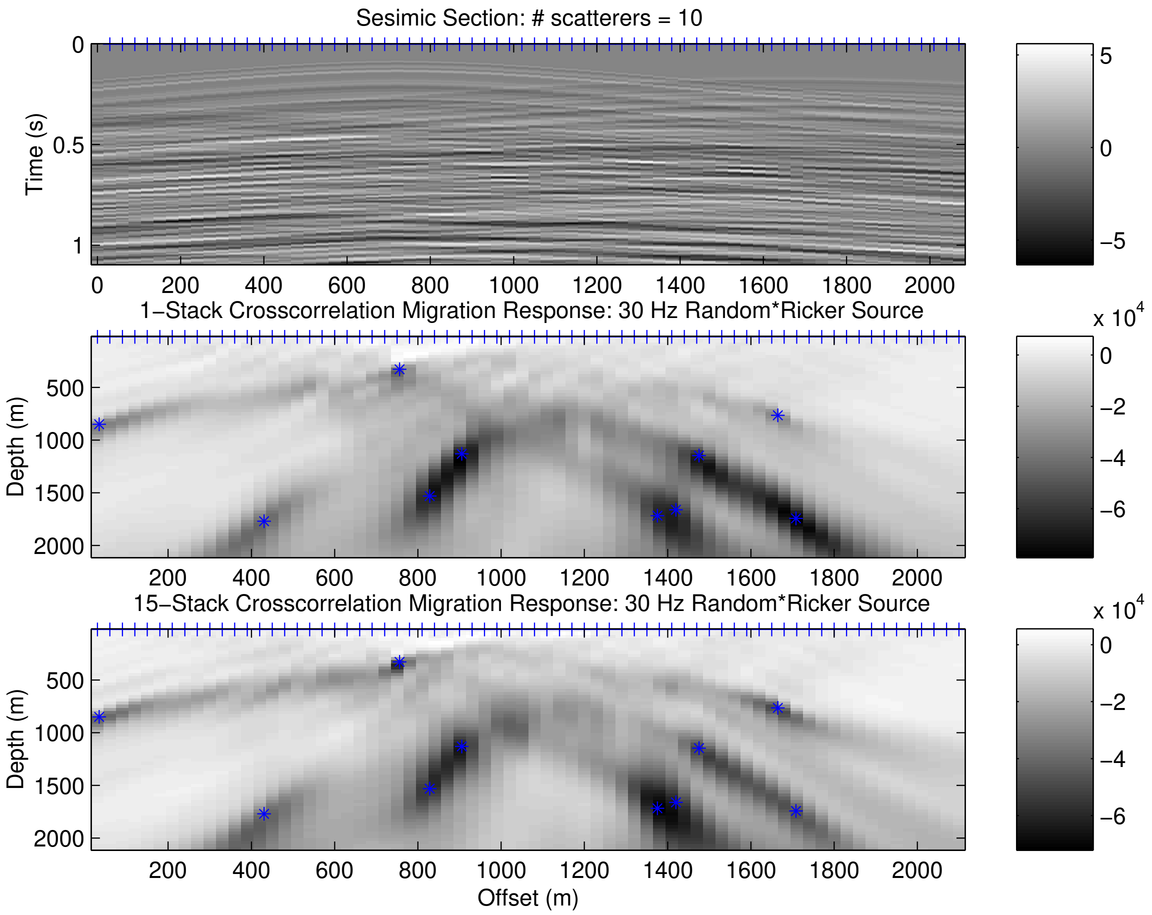

Figure 6: Similar to previous figures, except there are *ten* isolated random point sources (*). The top panel shows the synthetic data. The middle panel shows the crosscorrelation migrated image, computed from 1 second of data; while the bottom image shows the result after 15 stacks of 1-second data. The stacked image is better resolved because stacking tends to cancel noise and reinforce migration energy at the point exploder locations. schuster-fig6a [NR]

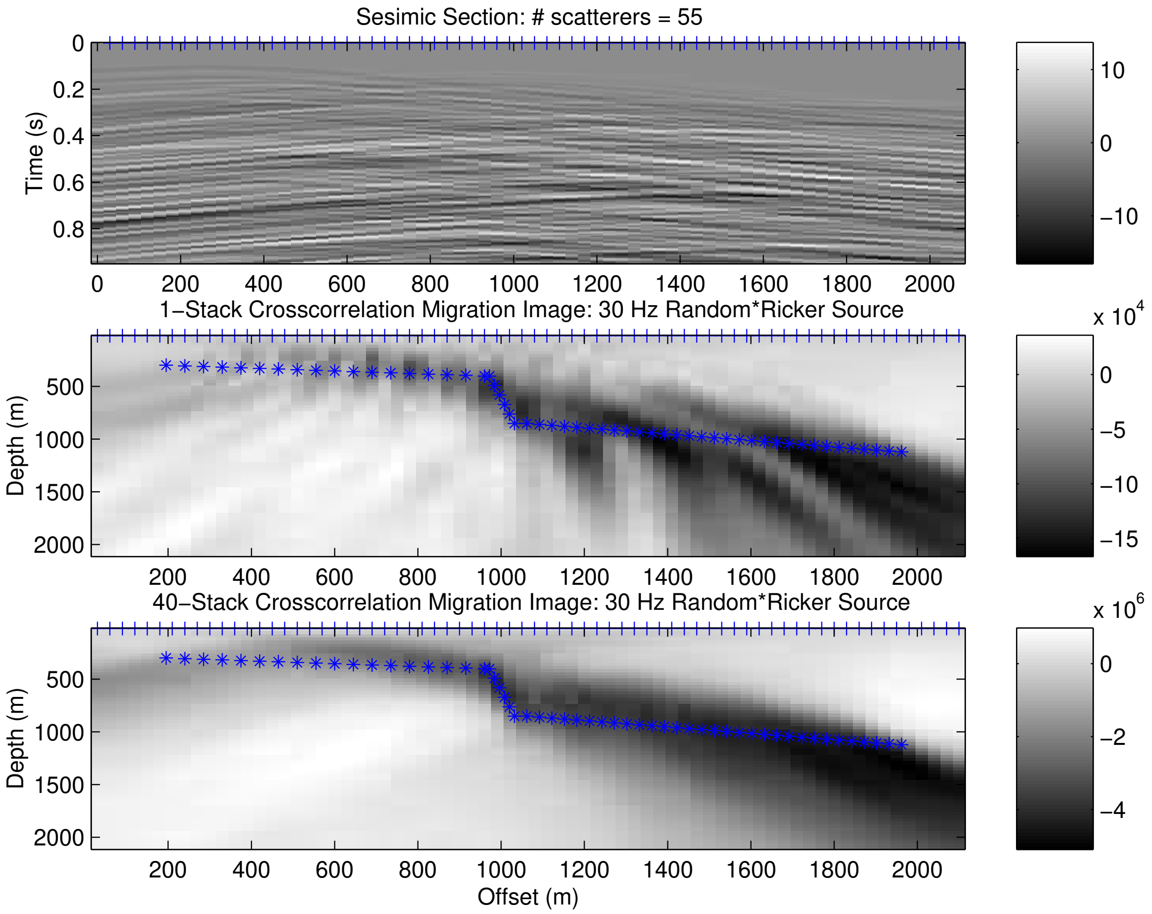

Figure 7: (Top). Source imaging test with 55 point exploders located along a fault-like boundary. The points exploded at random times with random weighting amplitudes. The top panel shows the synthetic data. The middle panel shows the crosscorrelation migrated image, computed from 1 second of data; while the bottom image shows the result after 40 stacks of 1-second data. The stacked image appears to be less noisy and a better approximation to the fault geometry delineated by stars. schuster-f7 [NR]

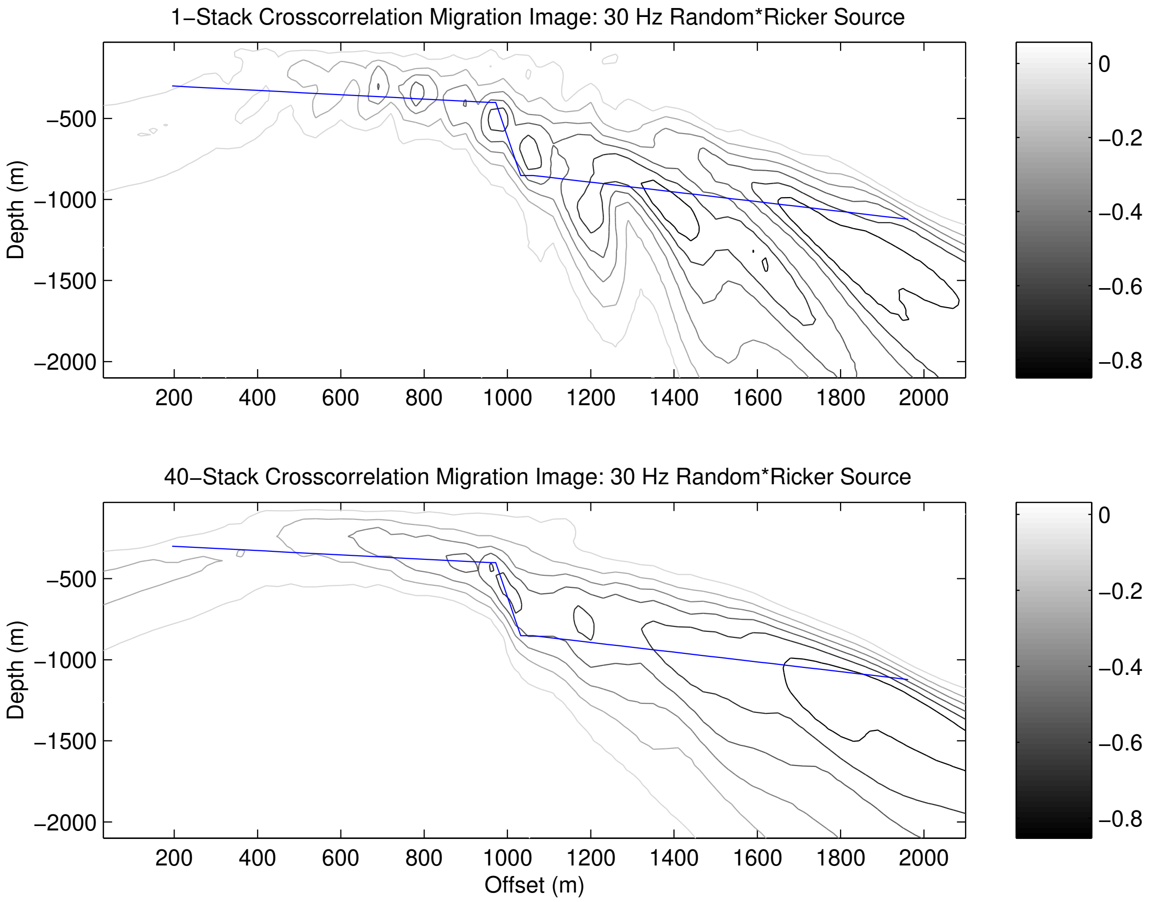

Figure 8: Similar to previous figure except the migration images are contoured, and the fault boundary is delineated by a dashed line. The top panel shows the crosscorrelation migrated image, computed from 1 second of data; while the bottom image shows the result after 40 stacks of 1-second data. schuster-fb [NR]

Imaging the reflectivity from free-surface reflections

A single impulsive source is located somewhere in depth, and the synthetic data generated in a 4-layer channel model are shown at the top of Figure 9. The interface boundaries are delineated by the dash-dot lines in the bottom figure, including the semi-circle river channel along the third interface. Using the migration operator for ghost reflections given by equation 6, the data are migrated to give the image at the bottom of Figure 9. Note, the source location was unknown, represented by the star symbol in the left bottom part of the migration image. It might be surprising that the single source generates enough data so that the model is almost entirely imaged. Part of the reason for this is that the ghost reflections illuminate a much greater part of the medium (for a fixed recording array) than primary reflections alone. Each point on the free surface acts as a virtual source.

Finally, ten point sources are buried at intermediate depths and their emissions are recorded on the surface. Each source is governed by a distinct random time series. Applying the migration operator for free-surface reflections [equation (6)] to the data shown at the top of Figure 10 yields the result shown in the bottom figure. Fifty one-second records were migrated and stacked with one one another, and show that the sand channel boundary is well imaged.

DISCUSSION

We present a methodology for using daylight data to image source locations or reflector boundaries for $v(x,y,z)$ media. Traces are crosscorrelated in time to form the correlation kernel in equation (3), this kernel is weighted by the appropriate migration operator, and summation over the g and g' indices is carried out to give the migrated image. Our theoretical formulae partly validate the conjecture: a crosscorrelogram is a trace that can be migrated in the same fashion as a trace generated by a source at g and a receiver at g'.

Other possibilities can be explored using the mathematical formalism in this paper. It is straightforward to develop a non-linear inverse methodology by using crosscorrelation misfit functions and obtaining its gradient.

It is interesting to note the analogy of inverting correlograms with that of constructing holograms. Light intensity images are used to reconstruct holograms, which are images of the object polluted by noisy interference terms. Seismic correlograms can also be used to reconstruct images of the object, but the *other terms* in equation (3) suggest that the data are polluted by noisy interference terms. However, we can design migration operators to reconstruct the object function (e.g., reflectivity) or information from the interference terms (e.g., source locations). An alternative is to simultaneously reconstruct both coherent noise and signal models with least squares migration filtering.

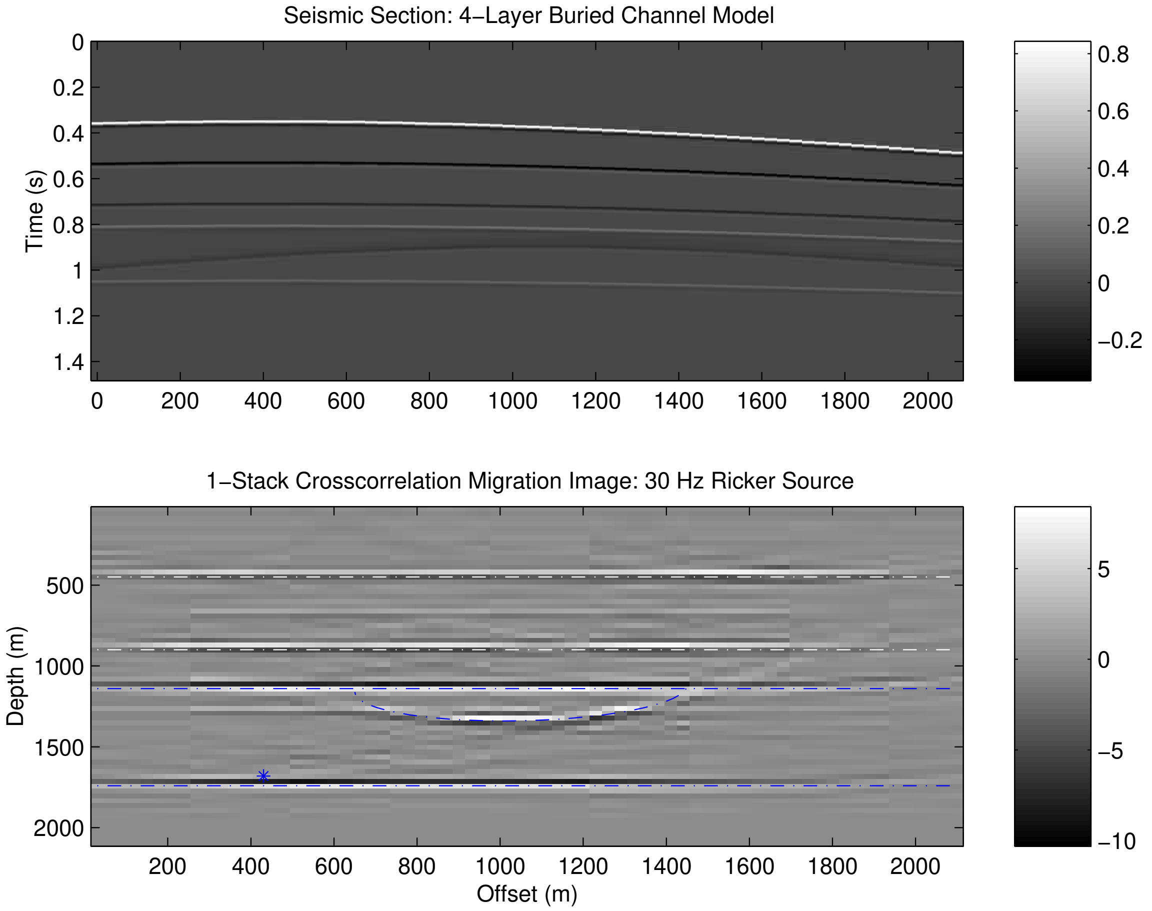

Figure 9: Similar to Figure 7 except now a a 4-layer sand channel model is imaged using one buried source. The source time history is a 30-Hz Ricker wavelet. schuster-f10 [NR]

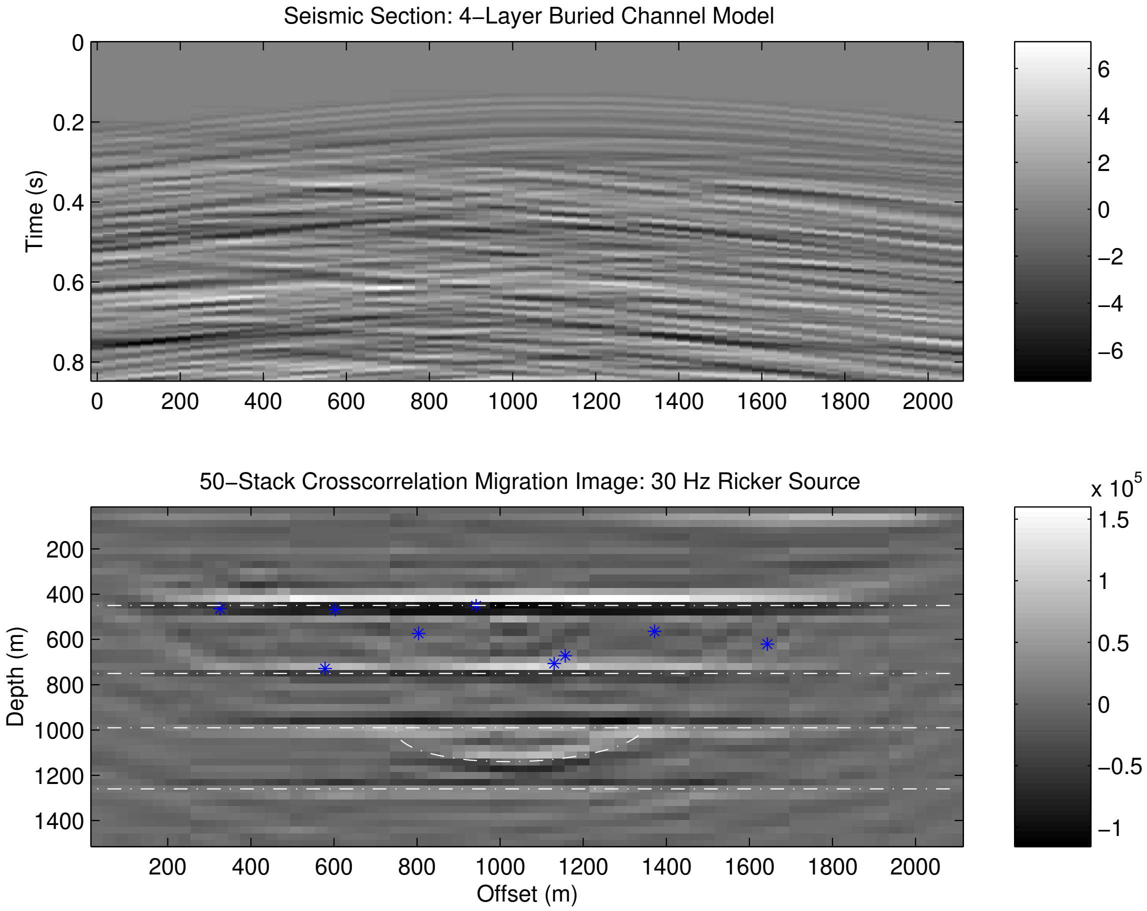

Figure 10: Similar to previous figure except there are now ten buried point sources scattered about at intermediate depths. Each source is governed by a distinct random time series. schuster-f12a [NR]

REFERENCES

Baskir, E., and Weller, C. E., 1975, Sourceless reflection seismic exploration: Geophysics, **40**, no. 1, 158–159.

Claerbout, J. F., 1976, Fundamentals of geophysical data processing: McGraw-Hill Book Co.

Cole, S., 1995, Passive seismic and drill-bit experiments using 2-D arrays: Ph.D. thesis, Stanford University.

Duvall, T. L., Jefferies, S. M., Harvey, J. W., and Pomerantz, M. A., 1993, Time-distance helioseismology: Nature, **362**, 430–432.

Giles, P. M., Duvall, T. L., and Scherrer, P. H., 1997, A subsurface flow of material from the sun's equator to its poles: Nature, **390**, 52.

Jack, I., and Thomsen, L., 1999, Recent advances show the road ahead for the electric oilfield very clearly: 69th Annual Internat. Mtg., Soc. Expl. Geophys., Expanded Abstracts, 1982–1983.

Kosovichev, A. G., 1999, Inversion methods in helioseismology and solar tomography: submitted to Elsevier Preprint.

Maxwell, S. C., Bossu, R., Young, R. P., and Dangerfield, J., 1998, Processing of induced microseismicity recorded in the Ekofisk reservoir: 68th Annual Internat. Mtg., Soc. Expl. Geophys., Expanded Abstracts, 904–907.

Rickett, J., and Claerbout, J., 1996, Passive seismic imaging applied to synthetic data: SEP–**92**, 83–90.

Rickett, J., and Claerbout, J., 1999, Acoustic daylight imaging via spectral factorization: Helioseismology and reservoir monitoring: The Leading Edge, **18**, 957–960.

Rickett, J. E., and Claerbout, J. F., 2000, Calculation of the acoustic solar impulse response by multi-dimensional spectral factorization: Solar Physics, **192**, no. 1/2, 203–210.

Rickett, J., 1996, The effects of lateral velocity variations and ambient noise source location on seismic imaging by cross-correlation: SEP–**93**, 137–150.

Scherrer, P. H., Bogart, R. S., Bush, R. I., Hoeksema, J. T., Kosovichev, A. G., Schou, J., Rosenberg, W., Springer, L., Tarbell, T. D., Title, A., Wolfson, C. J., Zayer, I., and the MDI Engineering Team, 1995, The Solar Oscillations Investigation - Michelson Doppler Imager: Solar Physics, **162**, no. 1/2, 129–188.

Schuster, G., Followill, F., Katz, L., Yu, J., and Liu, Z., 2000, Theory of autocorrelogram migration: submitted to Geophysics.

Schuster, G., 1999, Seismic interferometric imaging with waveforms: UTAM Midyear Report, pages 121–130.

Shapiro, S. A., Audigane, P., and Royer, J., 1999, Large-scale in situ permeability tensor of rocks from induced microseismicity: Geophys. J. Int., **137**, 207–213.

Yu, J., Katz, L., Followill, F., Sun, H., and Schuster, G., 2000, Autocorrelogram migration of IVSPWD data: submitted to Geophysics.